The Effect of Upstream Unsteadiness on the Unstarting of a Supersonic Inlet Turbine

Noraiz Mushtaq
Laboratory of Fluid Machines (LFM)
Department of Energy - Politecnico di Milano
Via Lambruschini 4, 20156 Milan, Italy
Email: noraiz.mushtaq@polimi.it

Paolo Gaetani*
Laboratory of Fluid Machines (LFM)
Energy Department - Politecnico di Milano
Via Lambruschini 4, 20156 Milan, Italy
Email: paolo.gaetani@polimi.it

ABSTRACT

A 15% increase in thermal efficiency at medium pressure ratios is promised by rotating detonation engine technology over conventional Joule-Bryton cycles. A supersonic inlet turbine is a viable option to extract substantial work from the highly fluctuating and supersonic flow delivered by the detonating combustor. However, an additional unstarting mechanism based on the generation of a collective shock from the coalescence of leading-edge bow-shock waves further restricts the available design space. Firstly, the effect of unsteady inlet conditions with variable frequency, amplitude, and mean value on collective shock generation is investigated. Then, a fast and cost-effective tool was developed and verified to predict bow shock wave motion from a prescribed inlet Mach trend; the parameters of the transfer function were estimated with a classical identification method based on a step-response CFD simulation. The model was employed to rapidly calculate the maximum amplitude of fluctuations accepted by the supersonic blade row for each frequency and average inlet Mach number. Finally, the influence of the inlet geometric angle, pitch to leading-edge thickness ratio, and static temperature on the model parameters is studied. The preliminary observations of the parametric analysis were confirmed by the rigorous

*Corresponding author.
TURBO-23-1248, Gaetani P.

quantitative approach of a global sensitivity analysis based on Sobol sensitivity indices.

Keywords: Rotating Detonation Engine (RDE); supersonic turbines; unstarting phenomena; shock wave dynamics

1 INTRODUCTION

Continuous growth in global energy consumption and climate change demand new solutions for clean and more efficient propulsion and power production devices. As for the land-based power systems, a substantial introduction of renewable – but unfortunately non-schedulable - technologies in the overall energy mix requires dedicated energy systems to assure stable grids operation. In this context, gas turbines, thanks to their flexibility and to the ability in using different fuels, represent a viable solution, ever more promising when integrated with rotating detonation combustors (RDC). In this technology, a detonation wave rotates typically in an annular chamber and burns the fresh mixture [1]. The pressure gain originated from the detonation wave allows for a decrease in fuel consumption [2, 3], an increase in total pressure (up to 15%) [4], an increase of gas turbine thermal efficiency [5, 6] and plant efficiency up to 14% over a conventional turbine [7] for intermediate pressure ratios. Rotating detonation engines (RDE) are also perfectly compatible with hydrogen, owing to its aptitude to detonation [8].

The RDC delivers transonic/supersonic and highly fluctuating flows making the design of an efficient turbine a very complex task. In this context, a transition duct, that connects the combustion chamber to the first turbine stage [9, 10] (either diffusing for a subsonic turbine or accelerating for a supersonic one) allows for a more efficient turbine design. This paper focuses on the design issues of supersonic inlet turbines and specifically on the sensitivity of the turbine design to the fluctuating inlet flow field.

Supersonic inlet turbines are characterized by large work extraction at the expense of lower efficiencies compared to subsonic designs. Detailed analysis of the 3D design of supersonic turbines were carried out by [11–13], where i) mean-line codes, ii) method of characteristics for the profile design, iii) high-fidelity CFD simulations, iv) shape optimization applied to endwalls, were combined to get a clear picture of the design complexity. Turbine interaction with the RDC was

investigated numerically by [14, 15] and experimentally by [16].
Supersonic inlet turbines need to comply with limitations characteristic of supersonic flows. Considering the unsteadiness of the incoming flow, the axial Mach number should be higher than sonic to avoid the unique incidence problem [17] and the self-starting condition must be always satisfied to obtain a configuration with bow-shock waves at the cascade inlet, which is less dissipative than the normal shock of the "unstarted" condition. The self-starting condition constrains the maximum contraction ratio in the channel [18], directly affecting the maximum allowable flow turning [12].

Furthermore, supersonic inlet turbines are constrained by an additional unstarting mechanism; this novel limit is based on the generation of a collective shock from the coalescence of the leading-edge bow shock waves; experimental evidence of this phenomenon has been provided by Boiko in his campaign of tests carried out on a shock tube [19]. The collective shock generated by a turbine blade row is straight and normal to the channel axis due to the periodicity; in addition, considering the flow orientation (not necessarily aligned to the channel axis), the collective shock behaves as an oblique shock wave, which turns the flow and reduces the effective area. However, a shock wave is unstable in a converging duct: the collective shock starts moving upstream in search for a stable position leading ultimately to the unstarting of the supersonic channel [20].
Shock wave merger depends on the shape of the bow shock waves and their intersection: in particular, low inlet Mach numbers, high inlet geometric angles or incidence angles are more vulnerable to collective shock unstarting. For example, Fig. 1 displays the sequence of shock structures from a regular intersection up to a collective shock as the inlet Mach number is progressively reduced. Failure to consider this additional limit during the design stage may have critical consequences, especially for the rotor which receives a lower inlet Mach number (diffusing stator channel) at non-zero inlet geometric angle.

Up to now, unstarting by collective shock was studied only with steady or quasi-steady flow conditions; since the flow delivered by a rotating detonation combustor is fluctuating at high frequency, it is deemed relevant to investigate the effect of unsteadiness on this additional unstarting mechanism. In particular, the present work aims at resolving the following open questions on this topic:

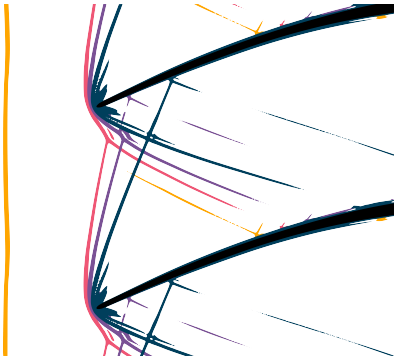

Fig. 1: SEQUENCE OF SHOCK STRUCTURES AS THE INLET MACH NUMBER IS PROGRESSIVELY REDUCED: FROM DARK TO LIGHT COLOURS, THERE ARE RESPECTIVELY A REGULAR INTERSECTION (IN BLUE), A MACH REFLECTION (IN PURPLE), A LAMBDA SHOCK (IN PINK) AND FINALLY A COLLECTIVE SHOCK (IN YELLOW).

i) What is the influence of the frequency, amplitude, and mean value of the prescribed inlet fluctuation on the generation of a collective shock?

ii) To avoid this phenomenon, a designer should consider only the average flow conditions or each of the instantaneous values assumed by the flow?

iii) For a given unsteady inlet condition, is it possible to predict if unstarting will or will not occur without an expensive CFD simulation?

To tackle these questions, the effects of unsteady inlet conditions were studied for variable frequency, amplitude, and mean value. Then, a second order model was developed and verified to predict shock wave dynamics with a cost-effective approach. Finally, a parametric and a global sensitivity analysis were carried out to assess the effect of the inlet geometric angle, pitch to leading-edge thickness ratio and static temperature on the model parameters.

2 COMPUTATIONAL FLOW MODEL

Ansys CFX was selected to conduct quasi-2D blade-to-blade computational fluid dynamics (CFD) simulations. The pressure-based implicit coupled solver was tested and proven to be accurate for supersonic flows against the Sod shock tube analytical solution [21] and the experimental data on a 2D compression corner [22, 23]. High-resolution total variation diminishing algorithms [24] were employed to model advection terms, while transient terms were discretized with a second order backward Euler scheme. Turbulence closure was achieved through the k-omega SST model and y^+ was kept below 1 on all wall surfaces. The working fluid was air which was

assumed to be a perfect gas.

Pressure, temperature, and velocity were all assigned at the supersonic inlet. Adiabatic and no-slip conditions were selected for the blade walls, while adiabatic and free-slip conditions were set for the hub and shroud walls. The outlet was supersonic, and the lateral boundaries were periodic.

Convergence was achieved when all residuals were below $5 \cdot 10^6$ at each time step (or the final step for a steady-state simulation). For the unsteady simulations with a periodic inlet, the convergence towards a periodic solution was assessed with Clark's methodology [25], which combines signal-processing techniques and fuzzy set theory. Further details on the periodic convergence analysis and on the time-step selection are reported in appendix A.

Structured grids with hexahedral cells, high orthogonality, and low skewness were generated by Ansys TurboGrid. The mesh independence was carried with the grid convergence index method [26]. For the blade-to-blade simulations (2 cells in radial direction), mesh grids with 334 thousand, 1 million, and 3 million cells were tested. The grid convergence index was calculated on the natural frequency of the second order system developed to predict shock wave dynamics from the data of a step-response CFD simulation (discussed in detail in Sec. 4); the 1 million cells mesh satisfied the independence condition with a grid convergence index from fine to medium mesh of 0.72%. It is relevant to observe that the grid independent mesh for blade row entropy production is 400k, which suggests that the study of bow-shock wave motion and collective shock formation demands more than twice the number of cells. Complete details about the case set-up and the solver validation are reported in [12].

3 THE EFFECT OF UNSTEADY INLET CONDITIONS

The flow delivered by the rotating detonation combustor and accelerated in the supersonic nozzle is still characterized by large unsteadiness at turbine inlet; hence, in addition to steady-state analyses, it is relevant to investigate shock wave dynamics and collective shock formation by accounting for the effect of fluctuating inlet conditions.

The Mach number was selected as oscillating variable, since this quantity plays a pivotal role in starting/unstarting phenomena and has a strong influence on the shock structures. The inlet Mach

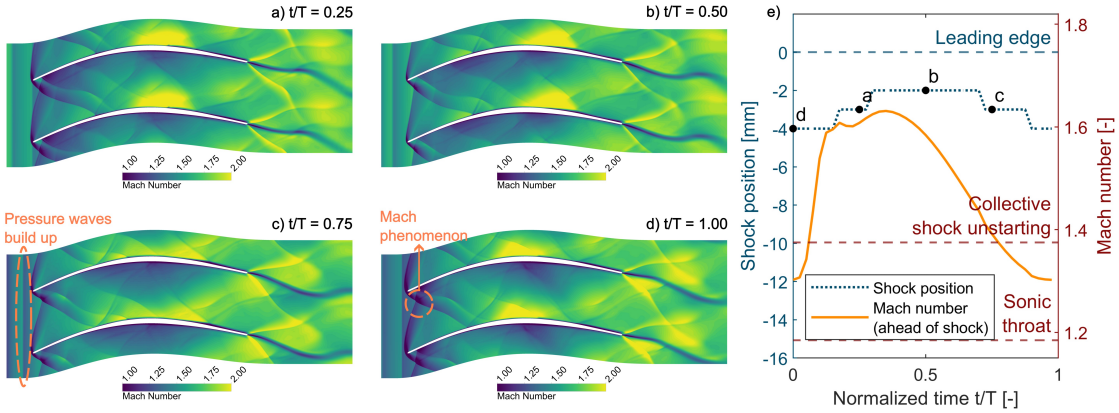

Fig. 2: MACH FIELD EVOLUTION IN A PERIOD CYCLE (a-d) FOR A SINUSOIDAL INLET MACH NUMBER FLUCTUATION WITH A FREQUENCY OF 6000 HZ (CASE 1) AND CORRELATION BETWEEN SHOCK POSITION AND MACH NUMBER EXTRACTED 2 MM AHEAD OF THE SHOCK (e).

number was varied in time with a sinusoidal function (Eq. 1), a shape proposed by Sousa et al. [27] to study supersonic turbine behavior when subjected to inlet angle fluctuations; inlet flow direction (25°), static pressure (1.92 bar) and static temperature (1300 K) were maintained constant.

$$M(t) = \bar{M} + Asin(2\pi ft) \tag{1}$$

To define the constants in Eq. 1, it is necessary to first select a turbine geometry. A value of 25° was selected for the inlet flow angle because a larger variety of features can be observed at this value. The outlet flow angle is half of the inlet flow angle, the stream-tube channel height ratio is 1.2 and the pitch to leading-edge thickness ratio is 42; these were all selected to avoid in all tested conditions the conventional unstarting by contraction ratio, i.e. the Kantrowitz limit. The supersonic profiles are generated with the “vortex-flow” method, which is an implicit Method Of Characteristics (MOC) developed by Goldman [28]. Since the MOC generated profile has infinitesimal thickness at the leading and trailing edge, the pressure side and suction side are shifted of a plausible thickness

Table 1: AVERAGE INLET MACH NUMBER, AMPLITUDE, FREQUENCY AND REDUCED FREQUENCY OF THE FIVE MOST RELEVANT CASES.

	$\bar{M}$ [-]	**A** [-]	**f** [Hz]	$\bar{f}$ [-]
Case 1 (Ref.)	1.465	0.204	6000	2.5
Case 2	1.465	0.240	600	0.25
Case 3	1.465	0.240	12000	5.00
Case 4	1.465	0.465	6000	2.50
Case 5	1.300	0.240	6000	2.80

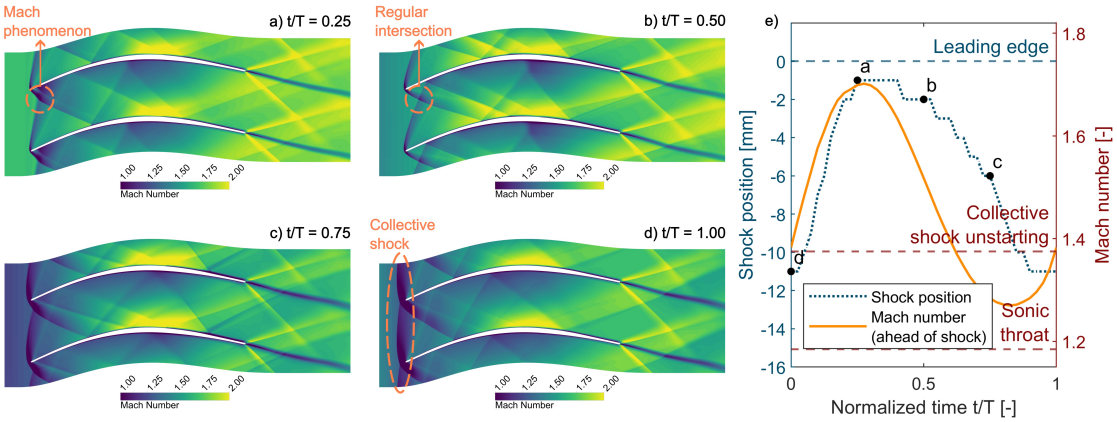

Fig. 3: MACH FIELD EVOLUTION IN A PERIOD CYCLE (a-d) FOR A SINUSOIDAL INLET MACH NUMBER FLUCTUATION WITH A FREQUENCY OF 600 HZ (CASE 2) AND CORRELATION BETWEEN SHOCK POSITION AND MACH NUMBER EXTRACTED 2 MM AHEAD OF THE SHOCK (e).

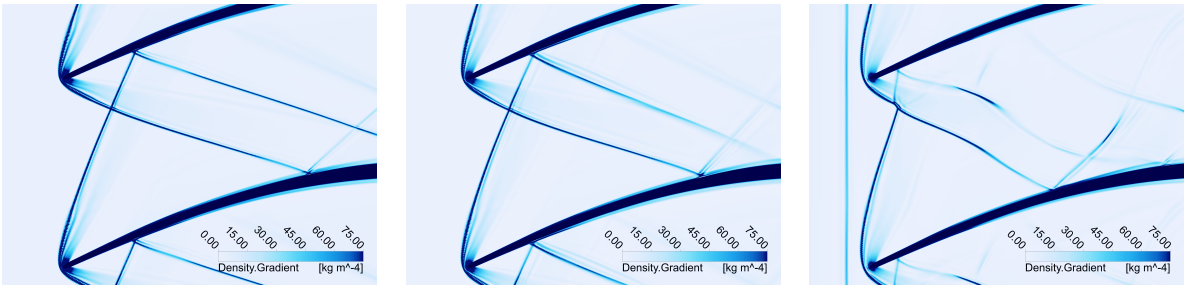

(a) steady-state (b) 600 Hz (c) 6000 Hz

Fig. 4: COMPARISON OF SHOCK STRUCTURES BETWEEN THE STEADY-STATE CASE (A) AND A SINUSOIDAL INLET MACH NUMBER FLUCTUATION WITH A FREQUENCY OF 600 HZ (B) AND 6000 HZ (C).

value and closed by ellipses. The inlet of the domain was placed only 1/8 of chord upstream of the leading edge to minimize flow mixing, which becomes relevant especially at large amplitude and at high frequencies. The proximity of the inlet boundary to the profile is not critical because the flow at inlet is always supersonic and the pressure information mainly travels downstream.

The mean value $\bar{M}$ of 1.465 is higher than the unstarting limit value of 1.375, which was determined by an unsteady simulation where the inlet Mach number was progressively reduced with a step-wise trend (Fig. 1); this choice aims at distinguishing if the supersonic blade row is just experiencing the mean value of the incoming flow or if it is also reacting to the instant values assumed by the sinusoidal function. The amplitude A was selected according to the unsteadiness levels reported by Braun et al. [10] at the outlet of a diverging nozzle (transition element designed to connect the RDC with supersonic inlet turbines); notice that the inlet Mach number falls for a

span of time under the unstarting limit by collective shock, but it is always larger than the Mach number for a sonic throat at the leading-edge. The frequency of the fluctuations delivered by the RDC is in the range of 1-10 kHz [14, 29–31]; thus, a frequency of 6 kHz [29] was selected for the definition of the reference inlet fluctuation.

Several inlet fluctuations, all featuring a sinusoidal pattern, with different values of frequency, amplitude and mean value were simulated. Five of these cases, outlined in table 1, will be presented in the paper as they condense all the essential information.

The frequency of the fluctuations is one of the driving parameters when a turbine is subjected to unsteady flow conditions. Case 1-3 compare how three different frequencies (6000 Hz, 600 Hz and 12000Hz) affect turbine behavior. The reduced frequencies $\bar{f}$, defined in Eq. 2, are respectively 2.5, 0.25 and 5.0. This quantity is typically employed to classify an unsteady problem: if the $\bar{f} << 1$, the flow is quasi-steady, while for $\bar{f} \geq 1$ the unsteady effects become more dominant [32]. A physical interpretation of the reduced frequency for this problem is the following: let's imagine that a fluid particle is starting from the inlet at the same time for the 600 Hz and the 6000 Hz case; in a period-time, the particle for the 600 Hz travels for 4 chords, while the particle for the 6000 Hz travels only for 0.4 chords. From this representation, it is immediately clear why the effect of unsteadiness will be more substantial in the case of 6000 Hz.

$$\bar{f} = \frac{f}{\frac{V_{\infty - x}}{c_x}} \tag{2}$$

The Mach field evolution with time for the 6000 Hz and the 600 Hz case is displayed in Fig. 2 and 3, respectively. In the 6000 Hz case, the flow field is characterized by large unsteadiness and the oblique shock waves are curved; this unusual shape is produced by the shock structures rapidly fluctuating back and forth, with the motion of the terminal portion of the shock delayed respect to the motion of the reflection point. Furthermore, the increase in pressure gradients due to the high frequency generate stronger pressure waves, which rapidly build-up as the flow travels from inlet up to the leading-edge (Fig. 2c). The most significant observation for the 6000 Hz case is that unstarting does not occur since collective shocks have not been generated: the inlet conditions are fluctuating so rapidly that the flow structures do not have sufficient time to adapt to the extreme

values; hence, for high reduced frequencies, the mean values are the driving parameter to assess whether unstarting by collective shock will occur.
On the contrary, unstarting by collective shock is observed for the 600 Hz. In each frame, the flow field has adjusted to the new inlet condition and the shock structures cyclically shift between regular intersection, Mach phenomenon and collective shock; in view of this, the lower frequency case manifests a quasi-steady behavior, as hinted by the reduced frequency value.

The relation between leading-edge bow shock waves intersection and frequency was further analyzed because these features are strictly connected to collective shock unstarting (Sec. 1). Figure 4 compares the shock structures at the maximum inlet Mach number obtained from a steady-state, 600 Hz and 6000 Hz simulations (for the unsteady cases, the extracted frames are the ones with the intersection point farthest from the leading edge). While the steady-state case and the 600 Hz one are almost identical, the flow field for the 6000 Hz is substantially different: in the intersection point of the 6000Hz case there is still a Mach phenomenon, which will never transform to a regular intersection because the shocks will start moving backwards in the next frames. Unstarting will occur only if the inlet Mach number remains below the starting limit for the extent of time required by the bow shock wave to adapt to the new inlet condition.

Bow-shock wave motion was tracked by means of control points placed in axial direction, 1 mm apart and ahead of the leading edge (Fig. 5). Studies have shown how unsteady shock wave dynamics to upstream disturbances is characterized by small scales at high frequency [33]. This statement is true also for this application, since the high frequency cases (1, 3 and 4) exhibit limited motion; in addition, as the frequency of the inlet fluctuation increases, the shock displacements become smaller. At 600 Hz (case 2), the displacement is considerably larger with the unstarting collective shock travelling upstream until it is pushed back by higher inlet Mach numbers. In the unsteady simulation, the exact inlet condition responsible for turbine unstarting are unclear, because it is complicated to distinguish between a collective shock marching towards the inlet boundary of the domain from a bow shock wave that is farther away from the leading edge just due to lower Mach numbers. On the contrary, the restart condition is definite, and it corresponds to the instant when the shock starts moving again towards the leading edge. Figure 3e reports the

shock position together with the Mach number just 2 mm ahead of the shock (case 2): as soon as the inlet Mach number goes above the starting limit, the shock starts moving towards the leading-edge and the supersonic channel restarts. This observation confirms that there is no hysteresis between starting and unstarting when the turbine operates with a quasi-steady flow.

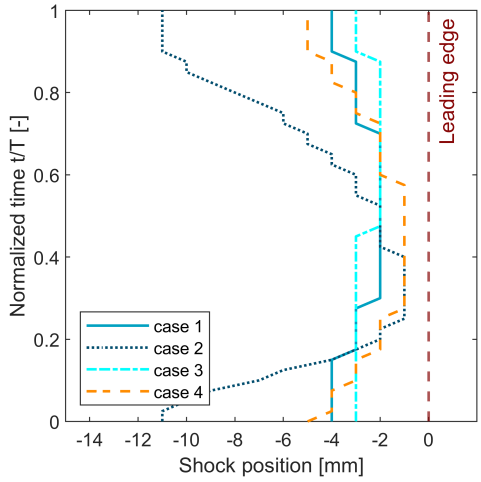

Fig. 5: BOW-SHOCK WAVE MOTION FOR CASE 1-4 TRACKED BY MONITOR POINTS PLACED IN AXIAL DIRECTION AHEAD OF THE LEADING EDGE. A NEGATIVE VALUE OF THE X AXIS CORRESPONDS TO A POSITION UPSTREAM OF THE LEADING EDGE.

In case 4, the amplitude was almost doubled, and the minimum inlet Mach number was lower than the Mach number for a sonic throat at the leading-edge. Nonetheless, unstarting did not occur, and the shock wave displacement slightly increased compared to the reference case (Fig. 5). This outcome is somehow expected since at high frequency the amplitude of the fluctuations becomes less significant, and the turbine is primarily reacting only to the mean flow conditions.

Finally, in case 5 the mean value $\bar{M}$ of the sinusoidal function was reduced below the unstarting limit. The simulation was initialized from a started flow condition (M = 1.465) and then the inlet Mach number started to oscillate around the lower mean value. The bow shock waves merged and formed a collective shock, which continued to march upstream until it reached the inlet.

4 MODELING BOW-SHOCK WAVE DYNAMICS

A collective shock is generated when the bow-shock waves during their motion intersect at a certain position which leads to their merger. Furthermore, the previous results revealed that shock displacement is damped for high frequency cases, since shock waves struggle to adapt to rapidly

changing inlet conditions. This characteristic can be beneficial especially for the high frequency flow released by the RDC, which would simplify the design process because only the mean values may be considered. Nonetheless, a fast and cost-effective tool is still required to assess whether a collective shock will appear for a prescribed inlet Mach number trend.

For this purpose, a simplified methodology was developed starting from the identification of the parameters of a second-order system that models shock wave dynamics. Then, the model capabilities were verified against the data extracted from accurate CFD simulations performed with different inlet conditions. Finally, the verified tool was employed to build parametric contour plots, that display the limit frequency, amplitude, and mean value responsible for collective shock unstarting.

4.1 Second-order system identification based on step-response

Several identification methods have been developed to estimate the parameters of a system or a transfer function from available input-output data [34]. The classical identification methods reconstruct the transfer function from a step-response. Hence, an auxiliary unsteady CFD simulation was carried out where the inlet Mach number was increased with a step from 1.465 to 2.

The increase in Mach number was not achieved through a velocity increase, but rather through a decrease in static temperature (Eq. 3). This alternative approach aimed at maintaining constant the mass-flow rate as the Mach number is varied: this option will be valuable especially for the simulations with fluctuating inlet conditions, since the mass-flow average Mach number before and after the mixing process will be the same.

$$\begin{cases} T(t) = \dfrac{V_0^2}{\gamma R M^2(t)} \\ p(t) = \left(\dfrac{T(t)}{T_0}\right) p_0 \\ V, \rho, \alpha \text{ constant} \end{cases} \tag{3}$$

The information about the increase of inlet Mach number travels on the right running characteristic (V+C) and arrives at the leading edge before the step front. These pressure waves obviously modify the shock position, but this has no repercussion on model identification since in a step

response the height of the step is not relevant (with the hypothesis of linearity of the model); the only condition to satisfy is that the bow-shock is already in a stationary position when the shock front reaches the blade, which was fulfilled by placing the blade row half a chord downstream of the inlet boundary. The blade profile is the same geometry described and employed in section 3.

Shock position was tracked by placing monitor points at intervals of 0.1 mm in axial direction along the mid-pitch line; this option was preferred over the previous one, because the same step in Mach number produces a smaller shift on the leading-edge line. Hence, a natural amplification of the signal is gained by placing the monitor points on the mid-pitch line, making the post-processing of data simpler and less sensitive to noise. Then, the shock location corresponds to the maximum of the density gradient [35].

The transfer function of a linear system G(s) is defined as the ratio between the output z and the input u (Eq. 4).

$$z(s) = G(s)u(s) \tag{4}$$

While z is the shock position, the input u cannot be the inlet Mach number, since the relation between the two variables is non-linear. There are two main reasons behind the non-linearity of this relation: first, the distance between the bow-shock and the leading edge is non-linear especially at low inlet Mach number [36]; secondly, the mid-pitch position of the monitor points further enhances the non-linearity (trigonometric functions). For example, an increase and a reduction of 0.25 at Mach 1.5 shifts the shock respectively by +13 mm and -24 mm.
This issue can be solved by transferring the information of the M(t) onto a new variable which is linear to the output z(t). The variable selected for this purpose is η(t) (input u of the system), which corresponds to the position reached by the shock if infinite time is provided to adapt to the inlet Mach number at time t. For each Mach number, η is determined through the method developed by Moeckel to predict the shape of a detached shock wave ahead of two-dimensional or axially symmetric bodies [36]; figure 6 displays such relation for the given geometry. The only but acceptable drawback of this approach is that the transformation from M(t) to η(t) and vice versa is viable only for supersonic inlet Mach number, which do represent most of the cases of interest.

Since a first order system was incapable of reproducing accurately the CFD step response, a

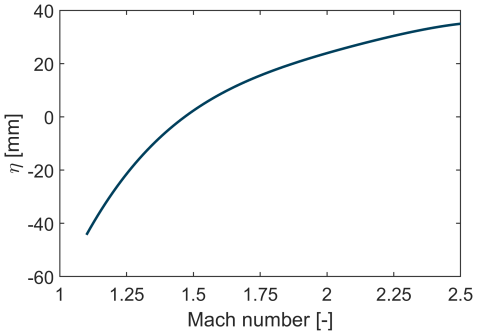

Fig. 6: NON-LINEAR RELATION BETWEEN THE INLET MACH NUMBER AND BOW-SHOCK POSITION ON THE MID-PITCH LINE IF INFINITE TIME IS PROVIDED TO ADAPT TO THE NEW INLET CONDITION.

generic second order system with one zero and two different poles was selected to model shock wave dynamics (Eq. 5). G(s) is characterized by a unitary gain because the steady shock position η and the actual dynamic shock position z coincide when η is changed slowly enough (quasi-steady process).

$$G(s) = \frac{1 + T_3 s}{(1 + T_1 s)(1 + T_2 s)} = \frac{1 + T_3 s}{1 + \frac{2\xi}{\omega_n} s + \frac{1}{\omega_n^2} s^2} \tag{5}$$

The parameters T_i of the system G are estimated through the procedure developed by Chen [34], which transforms the transcendental equations into a system of algebraic equations by evaluating the step response in special data points. The fundamental analytical steps of the derivation process to calculate model constants are reported in appendix B for sake of brevity.

Figure 7 compares the step response of the identified second order model with the shock wave dynamics extracted from the CFD: the model shows a good agreement with the CFD, especially for the slope of the ramp; however, there is a slight overshoot in the model prediction as the shock reaches the final position. This characteristic of the model can be explained by rewriting the complex conjugate poles in a more conventional form (Eq. 5), where ω_n is the undamped natural frequency and ξ is the damping ratio.

The system is underdamped because the damping ratio is 0.78, which explains the overshoot in the model response. Furthermore, the natural frequency of 4.727 kHz provides an immediate information on the shock wave dynamic behavior: if the frequency of the inlet fluctuation is lower than the natural frequency of the system, the shock wave will follow the prescribed signal with just

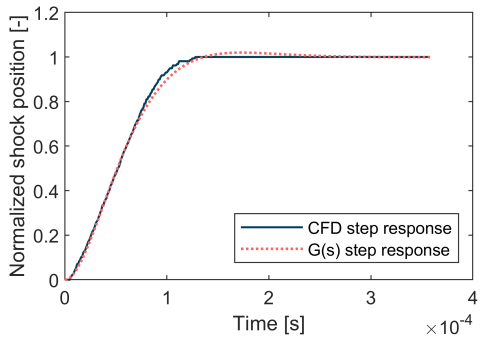

Fig. 7: STEP-RESPONSE COMPARISON BETWEEN THE MODEL AND THE CFD.

a delay; on the other hand, if the frequency of the inlet fluctuation is considerably higher than ω_n, the response of the shock wave will be severely filtered; in this sense, the dynamic of a shock wave is analogous to a second order filter.

4.2 Model verification with fluctuating inlet conditions

A campaign of unsteady simulations with fluctuating inlet conditions was carried out to verify the model and assess its predicting capabilities. Sinusoidal inlet conditions with variable frequency

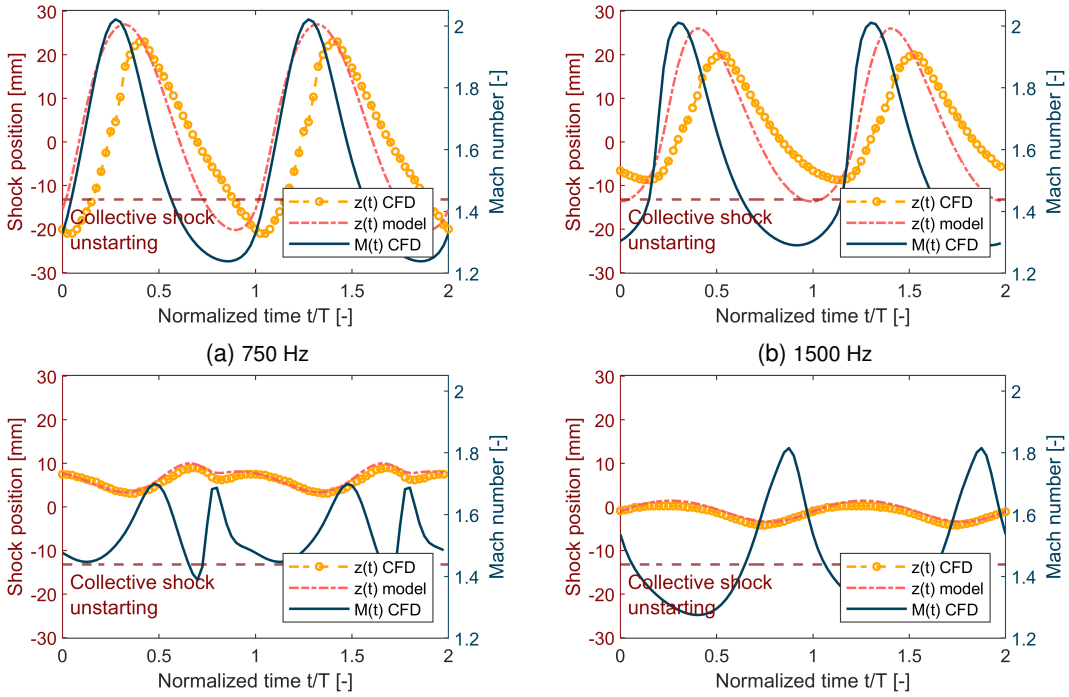

(a) 750 Hz (b) 1500 Hz

(c) 4500 Hz (d) 12000 Hz

Fig. 8: COMPARISON BETWEEN THE SHOCK WAVE DYNAMICS PREDICTED BY THE MODEL FROM THE η SIGNAL AND THE SHOCK POSITIONS EXTRACTED FROM CFD SIMULATIONS CARRIED OUT WITH FLUCTUATING INLET CONDITIONS.

were assigned, which satisfied Eq. 3 to maintain the mass-flow rate constant during the simulation.

The model requires accurate input data to accurately predict shock wave motion; hence, the inlet conditions cannot be considered adequate input for the model, because from the inlet boundary to the leading edge, the flow field has changed considerably due to mixing phenomena and right and left running characteristics travelling through the domain. Intuitively the reference location to extract the Mach signal should be closer to the leading edge, but not too close due to the shock wave oscillating back and forth. Since the time average Mach number remains constant from inlet up to the sections reached by the shock wave, the reference signal was extracted 5 mm ahead of the points characterized by a steep decrease in average Mach number.

The M(t) signal was then converted into η(t) through the non-linear transformation (Sec. 4.1). The η(t) signal has a generic shape, which requires some further steps to determine the output z(t). First, the signal was casted into an 8-term trigonometric Fourier series representation [37] (Eq. 6). Then, the frequency response theorem [38] was applied to each term of the Fourier series and the final signal was reconstructed by exploiting the linearity of the model (Eq. 7).

$$\eta(t) = a_0 + \sum_{n=1}^{8} a_n cos(n\omega_0 t) + b_n sin(n\omega_0 t) \tag{6}$$

$$z(t) = a_0 + \sum_{n=1}^{8} a_n |G(jn\omega_0)| cos(n\omega_0 t + \angle G(jn\omega_0)) + \sum_{n=1}^{8} b_n |G(jn\omega_0)| sin(n\omega_0 t + \angle G(jn\omega_0)) \tag{7}$$

Seven different frequencies (750 Hz, 1500 Hz, 3000 Hz, 4500 Hz, 6000 Hz, 9000 Hz and 12000 Hz) were tested and the results of four representative cases are displayed in Fig. 8. It is interesting to observe how the Mach number experienced by the supersonic blade row changes considerably as the frequency is increased. These variations are induced by the pressure and expansion waves generated by the fluctuating pressure signal: as the frequency is increased, the distance between two consecutive sinusoids is smaller and the pressure/expansion waves are stronger due to larger gradients. While the pressure waves naturally build-up leading to a steep decrease in Mach number, the expansion waves expand and increase the Mach number (Fig. 8b). These opposing effects lead to the double peak structure of Fig. 8c, where the smooth increase is associated to

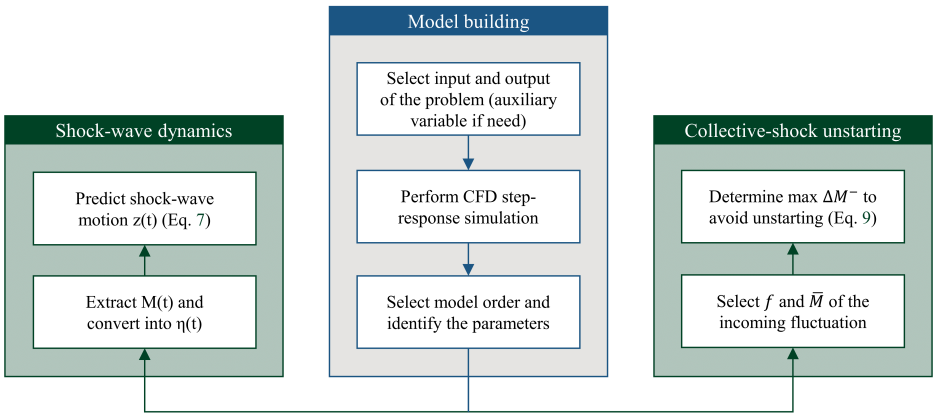

Fig. 9: FLOW CHART ILLUSTRATING THE NECESSARY STEPS TO BUILD AND APPLY THE MODEL.

the expansion waves and the steep one to the pressure waves. Ultimately, if the frequency is really high or sufficient distance is provided, the expansion wave reach and cancel the pressure waves generating a smooth Mach signal (Fig. 8d).

The correspondence between the shape predicted by the model and the CFD is striking both at low and at high frequency cases, even when the input Mach number is quite elaborate. At low frequency, the amplitude predicted by the model is slightly larger because the reference signal was extracted at a farther position from the leading edge due to a wide fluctuation of the shock; from that location to the leading edge, there is additional mixing which moderates the signal, and which is not accounted in the model. Furthermore, a farther reference location is also responsible for the time delay between the model and the CFD; however, this aspect is of secondary importance, because the focus was on reproducing accurately the shape and the amplitude of the shock wave motion. At high frequency, the agreement between the model and the CFD is excellent for the shape, the amplitude, and the delay in phase. Finally, a collective shock is generated at the lowest frequency case (750 Hz): this is revealed by the minimum shock position overcoming the minimum η, which is attainable only by a collective shock, which by its nature continues to travel upstream until higher Mach numbers are provided.

4.3 Model application

The methodology outlined in the flow chart (Fig. 9) and presented in Sec. 4.1 has great potential, since its application is not bounded only to the study of bow-shock wave dynamics, but

it can be easily extended to a variety of dynamic problems. For example, it can be employed to predict the dynamic load on a blade due to fluctuating inlet conditions (highly relevant for mechanical calculations). The limitation on model application to cases with a linear relation between input and output can be solved through the definition of an auxiliary variable, such as the non-linear transformation of M(t) into η(t) proposed by the authors; for this issue, a simple but effective approach would be to carry out a series of steady-state simulations to map each inlet condition to a steady response of the output; then, the relation between the dynamic output and the auxiliary variable obtained from the mapping will always be linear. In the field of bow-shock wave dynamics, shock position in time can be determined with only the trend of the Mach number seen by the leading edge; this significantly reduces the computational cost (lower number of cells needed) and alleviates user effort in simulation set-up and data post-processing.

Sousa et al. [27] have also developed a model to estimate outlet conditions when a supersonic passage is exposed to pulsating inlet conditions. While Sousa's model, based on a running average of the steady-data, requires only the steady state CFD simulations and the dynamic input, our model requires an additional step-response CFD simulation to identify the parameters of the transfer function. However, the main advantage of our model lies in its ability to accurately predict not only the amplitudes, but also the entire output signal, including its shape and the complete frequency content; this additional data is extremely relevant in dynamic problems. Moreover, the application of our model is not limited to supersonic flows.

For the unstarting problem, the model can be applied to determine the maximum amplitude of fluctuations accepted by the supersonic blade row without the generation of a collective shock. For simplicity, let's consider that the input η is a generic sinusoidal function, which depends on the average inlet Mach number $\bar{M}$ and on the frequency f (Eq. 8).

$$\eta(t) = \bar{\eta}(\bar{M}) + \Delta\eta sin(2\pi f t) \tag{8}$$

Since the two shock waves merge when the lower blade shock reaches -13.2 mm on the mid-pitch line (determined from the quasi-steady simulation) and the average shock position $\bar{z}(\bar{M})$ coincides with $\bar{\eta}(\bar{M})$, the maximum amplitude of the input fluctuation can be determined by exploiting the

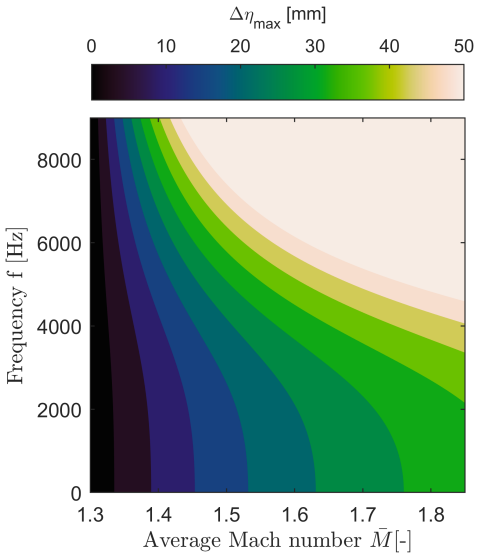

Fig. 10: MAXIMUM AMPLITUDE OF $\Delta\eta$ ACCEPTED BY THE SUPERSONIC BLADE ROW WITHOUT THE GENERATION OF A COLLECTIVE SHOCK.

frequency response theorem [38] (Eq. 9).

$$\Delta\eta_{max} = \frac{|\bar{z}(\bar{M}) - z_{unstart}|}{|G(j2\pi f)|} \tag{9}$$

Figure 10 shows the results of a parametric analysis carried out on a range of average Mach numbers and frequencies. For lower frequencies, the damping between the input η and the output z is negligible with a quasi-steady behavior of the shock wave. As the frequency is progressively increased, the blade row can accept larger and larger fluctuations for the same average Mach number. It is interesting to observe that very high frequencies with large average inlet Mach numbers allow extremely large amplitude of the fluctuations, up to the limit of acceptability of the model itself; nonetheless, the possibility of collective shock unstarting is very unlikely in these conditions.

Since the results in the form of $\Delta\eta$ can be less intuitive, the data were transformed from $\Delta\eta$ to ΔM^{-}, which is calculated as the difference between the average Mach number and the minimum Mach number corresponding to the minimum η, i.e. the minimum shock position (Fig. 11). As explained in Sec. 4.1, this variable change is allowed only for supersonic Mach numbers, which excludes the extremely large fluctuations in the right upper corner. For lower frequencies, the minimum Mach number in the sinusoid corresponds to the steady-state Mach number for collective shock unstarting. For higher frequencies, the inlet Mach number during its fluctuation can reach

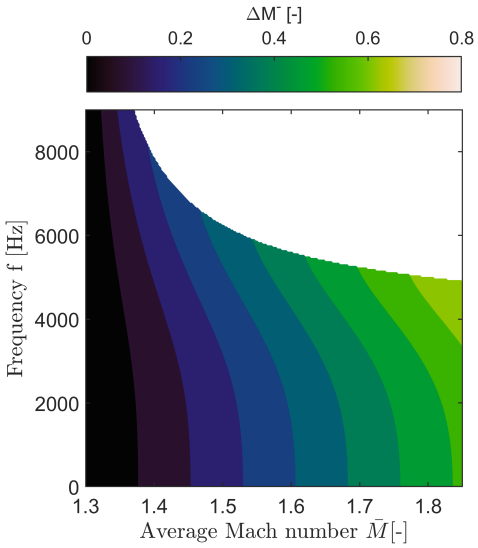

Fig. 11: MAXIMUM AMPLITUDE OF ΔM^- ACCEPTED BY THE SUPERSONIC BLADE ROW WITHOUT THE GENERATION OF A COLLECTIVE SHOCK.

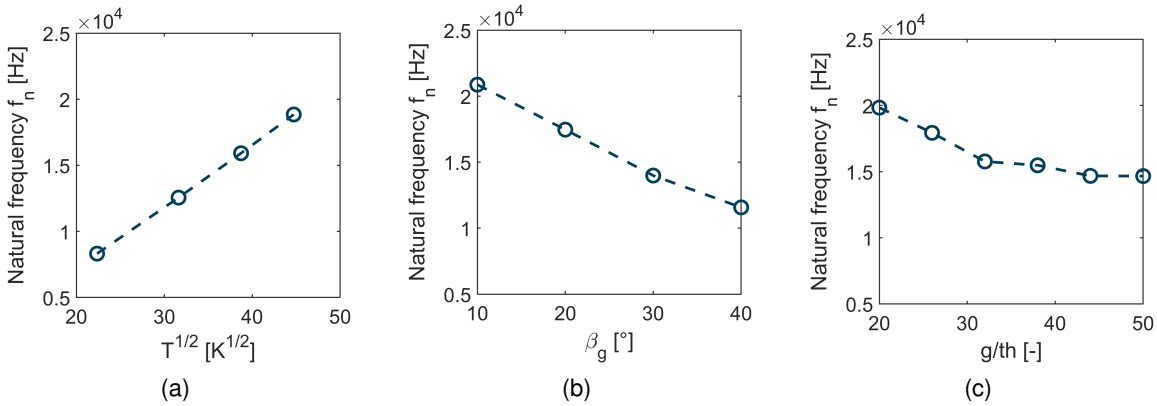

Fig. 12: CORRELATION BETWEEN THE UNDAMPED NATURAL FREQUENCY OF THE MODEL AND THE STATIC TEMPERATURE (A), THE INLET GEOMETRIC ANGLE (B) AND THE PITCH TO LEADING EDGE THICKNESS RATIO (C).

lower values than the steady collective shock limit thanks to the damping in the shock wave dynamics. For example, for an average Mach number of 1.5, the minimum Mach number is 1.3 at 0 Hz and 1.16 at 6000 Hz (ΔM^- is respectively 0.2 and 0.34, which represents a 70% increment).

In conclusion, these charts can be a useful tool in the design of a supersonic turbine to rapidly assess if a geometry suffers or not from this type of unstarting without an expensive CFD simulation and to evaluate how safe it is from the limit condition.

5 PARAMETRIC AND SENSITIVITY ANALYSIS

In section 4, a methodology to predict shock wave dynamics based on a second-order model was developed, and its constants were identified through a step-response CFD simulation. However, the values of the natural frequency and the damping ratio obtained for the specific geometry cannot be used for a generic supersonic blade row. In this final section, the sensitivity of the model to relevant design parameters is investigated.

First, a parametric analysis was carried out on three parameters: the inlet geometric angle, the pitch to leading-edge thickness ratio and the static temperature; the two geometric parameters were selected based on their critical influence on the steady-state collective shock unstarting limit, while the temperature was chosen because it is proportional to the speed of sound and consequently to the speed of propagation of the perturbations.

For the step definition, the inlet Mach number was raised from Mach 2 to 2.5; these values are higher to avoid the generation of a collective shock in the case of large inlet geometric angles and small pitch to leading-edge thickness ratios. The remaining boundary conditions are calculated from Eq. 3, which maintains a constant mass-flow rate during the simulation. The initial static pressure (before the step) was determined to achieve Reynolds number similarity to a reference case.

The results of the parametric analysis are resumed in Fig. 12. The natural frequency of the model is linear with the square root of the static temperature: this outcome is logical because the speed of sound in a perfect gas is $C = \sqrt{\gamma RT}$; hence, if the static temperature is increased, the perturbations travel faster, and the bow shock is able to adapt more rapidly to new inlet conditions. As β_g is increased, the angle between the bow shock and the axial direction is larger leading to a wider pitch-wise extension of the shock; the penetration of the flow inside the channel is reduced by the shock front, which justifies the slower reaction time for high inlet geometric angles.
The distance from the leading edge to the mid-pitch line increases for larger pitch to leading edge thickness ratios. Since the shape of the bow shock is dictated by the leading edge, the frequency of the shock wave dynamics reduces as the mid-pitch line gets farther.

The weakness of this parametric analysis is that each variable was changed one at a time,

while the other two were kept fixed; since the observations cannot be generalized on the entire parametric design space, it was decided to perform a global sensitivity analysis. The influence of each parameter on the natural frequency was quantified by means of Sobol' sensitivity indices; these indices measure the part of the output's variance due to one or more inputs [39] (analysis of variance). The most rigorous statistical approach to calculate them (Monte Carlo method) demands an extremely large number of evaluations, which is unfeasible considering the high computational cost of each CFD simulation (each evaluation takes around 4 hours on a 40-core intel Xeon Gold 6242R CPU). Meta-modeling methods have proven to be computationally more efficient, as they rely on a lower number of model evaluations [40]. In this work, the meta-model selected to calculate the Sobol' sensitivity indices was polynomial chaos (PC) expansion.

The number P of basis function can be calculated with Eq. 10, where p and d are respectively the order of the PC expansion and the number of the parameters.

$$P = \frac{(p+d)!}{p!d!} \tag{10}$$

Furthermore, Hadigol recommends an oversampling ratio 3-4 times larger than the number of the PC coefficients P for a small order polynomial [41]. With a third-order degree polynomial and an oversampling ratio of 3, the number of necessary samples is equal to 60. The Orthogonal Matching Pursuit (OMP) algorithm proposed by Pati et al. [42] and implemented in the UQLab module [43] was then employed to calculate the coefficients.

Profiles with inlet geometric angles spanning from 0° to 40° were generated, the pitch to leading edge thickness ratio was varied between 20 and 50 and the minimum and maximum static temperatures are respectively 500 K and 2000 K; within this ranges, a uniform probability distribution was assumed for each parameter. Latin Hypercube Sampling (LHS) technique was applied to generate the 60 samples from equiprobable partitions of the sample space. Considering the high number of computations, a completely automatized procedure was developed: the description of such procedure is omitted for sake of brevity, as it does not constitute novelty. The results of 3 out of the 60 samples were removed, because optimal residual convergence was not achieved for each step time.

A further set of 8 samples was generated with LHS and simulated for validation purposes (Fig. 13); there is satisfactory agreement between the frequency predicted by the PC expansion and the values extracted from the CFD simulation (validation error 0.97%), while the error bars correspond to the leave-one-out cross-validation error of 5.75% [44]. Higher order PC expansions with larger oversampling ratios would provide better accuracy at the expense of a substantial increase in computational cost; in the authors' opinion, the third order polynomial with 60 samples represented indeed an acceptable compromise between accuracy and simulation time.

Finally, Fig. 14 displays the total Sobol indices of the undamped natural frequency of the bow

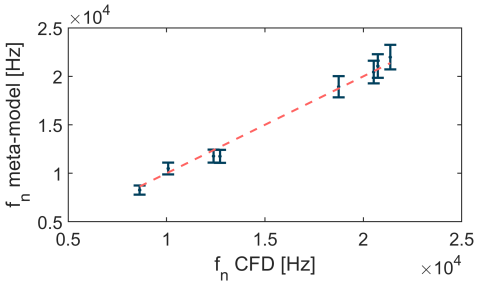

Fig. 13: META-MODEL VALIDATION ON A SET GENERATED WITH LATIN HYPERCUBE SAMPLING. THE ERROR BARS CORRESPOND TO THE LEAVE-ONE-OUT CROSS-VALIDATION ERROR.

shock wave dynamic model. These indices provide a global quantitative measure of the effect of a single parameter and its interaction with all the others. The weight of the static temperature and the inlet geometric angle is more than twice the weight of the pitch to leading edge thickness ratio. For example, a designer can improve safety from unsteady collective shock unstarting by lowering the static temperature, which will reduce the natural frequency and damp shock wave motion due to fluctuations of η at high frequency (typical of RDEs). In the same way, if the pitch to leading edge thickness ratio is adjusted in a later design phase, the effect on shock wave dynamics will be only secondary. In conclusion, the results of the global sensitivity analysis confirm with a quantitative approach the preliminary observations of the parametric analysis.

6 CONCLUSIONS

Unstarting by collective shock introduces an additional constraint on the design of supersonic inlet turbines for rotating detonation engines. This paper investigates the effect of unsteady inlet conditions on bow-shock wave dynamics and collective shock generation by means of URANS

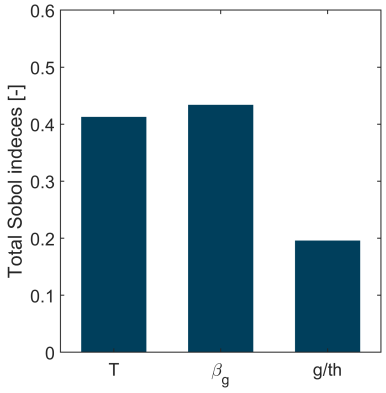

Fig. 14: TOTAL SOBOL INDICES FOR THE ANALYSIS OF VARIANCE OF THE UNDAMPED NATURAL FREQUENCY OF THE BOW SHOCK WAVE DYNAMIC MODEL.

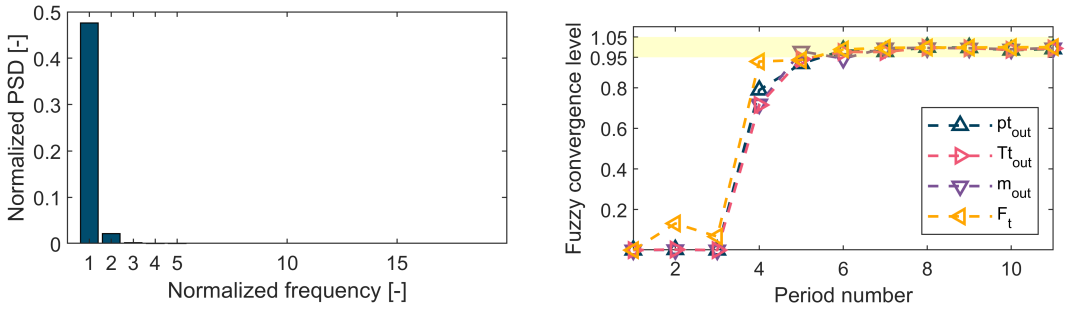

Fig. 15: NORMALIZED POWER SPECTRAL DENSITY OF THE MASS-FLOW AVERAGE OUTLET TOTAL PRESSURE (A) AND OVERALL FUZZY CONVERGENCE LEVEL FOR INCREASING PERIOD NUMBER (B).

CFD simulations. For frequencies lower than the natural frequency of the system, the bow shock wave adjusts to each new inlet condition and the flow has a quasi-steady behavior in the supersonic channel; on the contrary, for frequencies far greater than the natural frequency, the flow structures do not have sufficient time to adapt, and the mean values become the primary parameter to assess whether the unstarting by collective shock will occur.

An original model was developed to predict shock wave dynamics without expensive CFD simulations; the parameters of the model were identified through a CFD step-response simulation. The model was verified against data extracted from unsteady simulations with inlet conditions fluctuating at seven different frequencies. The agreement between the shape and amplitude of shock wave motion predicted by the model with the CFD is excellent both for low and high frequencies. Contour charts reporting the maximum acceptable amplitude of fluctuations for each frequency and average Mach number constitute a valuable tool for the design of a supersonic

turbine. For lower frequencies, the minimum Mach number corresponds to the steady-state limit for collective shock unstarting, while for higher frequencies lower values of the inlet Mach number can be reached due to the damping in shock wave motion. The application of the proposed methodology transcends the field of bow shock wave motion to a variety of dynamic problems: the only requirements are a step-response CFD simulation to identify model parameters and a series of steady-state simulations for the mapping procedure if a non-linear relation exists between input and output.

Finally, the sensitivity of the model parameters was assessed first with a parametric analysis and then with a global sensitivity analysis based on total Sobol indices. The parameter considered were the static temperature, the inlet geometrical angle and the pitch to leading edge thickness. The study revealed that the variance of the inlet geometric angle and the static temperature is more than twice the variance of the pitch to leading-edge thickness ratio.

NOMENCLATURE

A	Amplitude of the fluctuation [-]
C	Speed of sound [ms^{-1}]
c	Chord [m]
d	Number of parameters [-]
f	Frequency [Hz]
$\bar{f}$	Reduced frequency [-]
G	Transfer function [-]
M	Mach number [-]
p	Pressure or polynomial order [Pa or -]
P	Basis of PC expansion [-]
t	Time [s]
T	Temperature or period of a cycle [K or s]
T_i	Dynamic model constants [-]
u	Input [-]
V	Velocity [ms^{-1}]

z Shock wave position [m]

α Absolute flow angle [deg]

β_g Geometric angle [deg]

γ Specific heat ratio [-]

ρ Density [kgm^{-3}]

η Steady-state shock position [m]

ξ Damping ratio [-]

ω_n Natural frequency of the model [$rad\ s^{-1}$]

Subscripts

∞ Upstream conditions

0 Initial conditions

1,2 Blade row inlet and outlet, respectively

x Axial

Acronyms

CFD Computational Fluid Dynamics

LHS Latin Hypercube Sampling

MOC Method of Characteristics

PC Polynomial Chaos

PSD Power Spectral Density

RDC Rotating Detonation Combustor

RDE Rotating Detonation Engine

REFERENCES

[1] Wolański, P., 2013, "Detonative propulsion," *Proceedings of the Combustion Institute,* **34**(1), pp. 125–158.

[2] Jones, S. M., and Paxson, D. E., 2013, "Potential Benefits to Commercial Propulsion Systems from Pressure Gain Combustion," In *49th AIAA/ASME/SAE/ASEE Joint Propulsion Conference*, Joint Propulsion Conferences. American Institute of Aeronautics and Astronautics, jul.

[3] Wintenberger, E., and Shepherd, J. E., 2006, "Thermodynamic Cycle Analysis for Propagat-

ing Detonations," *Journal of Propulsion and Power,* **22**(3), may, pp. 694–698.

[4] Frolov, S. M., Dubrovskii, A. V., and Ivanov, V. S., 2013, "Three-dimensional numerical simulation of operation process in rotating detonation engine," *Progress in Propulsion Physics,* **4**, pp. 467–488.

[5] Sousa, J., Paniagua, G., and Collado Morata, E., 2017, "Thermodynamic analysis of a gas turbine engine with a rotating detonation combustor," *Applied Energy,* **195**, pp. 247–256.

[6] Strakey, P., Ferguson, D., Sisler, A., and Nix, A., 2016, "Computationally Quantifying Loss Mechanisms in a Rotating Detonation Engine," In *54th AIAA Aerospace Sciences Meeting*, AIAA SciTech Forum. American Institute of Aeronautics and Astronautics, jan.

[7] Claflin, S., Sonwane, S., Lynch, E., and Stout, J., 2014, "Recent advances in power cycles using rotating detonation engines with subcritical and supercritical CO2," In 4th International Symposium - Supercritical CO2 Power Cycles.

[8] Anand, V., and Gutmark, E., 2019, "Rotating detonation combustors and their similarities to rocket instabilities," *Progress in Energy and Combustion Science,* **73**, pp. 182–234.

[9] Braun, J., Saracoglu, B. H., and Paniagua, G., 2017, "Unsteady performance of rotating detonation engines with different exhaust nozzles," *Journal of Propulsion and Power,* **33**(1), pp. 121–130.

[10] Braun, J., Paniagua, G., and Ferguson, D., 2021, "Aero-Thermal Characterization of Accelerating and Diffusing Passages Downstream of Rotating Detonation Combustors," In ASME Turbo Expo 2021, pp. GT2021–59111.

[11] Paniagua, G., Iorio, M. C., Vinha, N., and Sousa, J., 2014, "Design and analysis of pioneering high supersonic axial turbines," *International Journal of Mechanical Sciences,* **89**, pp. 65–77.

[12] Mushtaq, N., Colella, G., and Gaetani, P., 2022, "Design and Parametric Analysis of a Supersonic Turbine for Rotating Detonation Engine Applications," *International Journal of Turbomachinery, Propulsion and Power,* **7**(1).

[13] Mushtaq, N., Persico, G., and Gaetani, P., 2023, "The Role of Endwall Shape Optimization in the Design of Supersonic Turbines for Rotating Detonation Engines," *Journal of Turbomachinery,* **145**(8), may.

[14] Liu, Z., Braun, J., and Paniagua, G., 2019, "Characterization of a Supersonic Turbine Downstream of a Rotating Detonation Combustor," *Journal of Engineering for Gas Turbines and Power,* **141**(3), pp. 1–13.

[15] Shen, D., Cheng, M., Wu, K., Sheng, Z., and Wang, J., 2022, "Effects of supersonic nozzle guide vanes on the performance and flow structures of a rotating detonation combustor," *Acta Astronautica,* **193**, pp. 90–99.

[16] Bach, E., Bohon, M. D., Paschereit, C. O., and Stathopoulos, P., 2019, "Influence of nozzle guide vane orientation relative to RDC wave direction," In AIAA Propulsion and Energy Forum and Exposition, 2019.

[17] Starken, H., Yongxing, Z., and Schreiber, H.-A., 1984, Mass Flow Limitation of Supersonic Blade Rows due to Leading Edge Blockage, jun.

[18] Kantrowitz, A., and Donaldson, C., 1945, "Preliminary inversitagtion of supersonic diffusers," *NACA Wartime reports*.

[19] Boiko, V. M., Klinkov, K. V., and Poplavskii, S. V., 2004, "Collective Bow Shock Ahead of a Transverse System of Spheres in a Supersonic Flow Behind a Moving Shock Wave," *Fluid Dynamics,* **39**(2), pp. 330–338.

[20] Mushtaq, N., and Gaetani, P., 2023, "Understanding and modeling unstarting phenomena in a supersonic inlet cascade," *Physics of Fluids*.

[21] Sod, G. A., 1977, "A numerical study of a converging cylindrical shock," *Journal of Fluid Mechanics*.

[22] Settles, G. S., and Dodson, L. J., 1991, "Hypersonic shock/boundary-layer interaction database," In AIAA 22nd Fluid Dynamics, Plasma Dynamics and Lasers Conference, 1991.

[23] Settles, G., and Dodson, L., 1994, "Hypersonic shock/boundary-layer interaction database: new and corrected data," *Pennsylvania State Univ. Report*.

[24] Druguet, M. C., and Zeitoun, D. E., 2003, "Influence of numerical and viscous dissipation on shock wave reflections in supersonic steady flows," *Computers and Fluids*.

[25] Clark, J. P., and Grover, E. A., 2006, "Assessing Convergence in Predictions of Periodic-Unsteady Flowfields," *Journal of Turbomachinery,* **129**(4), aug, pp. 740–749.

[26] Celik, I. B., Ghia, U., Roache, P. J., Freitas, C. J., Coleman, H., and Raad, P. E., 2008, "Procedure for estimation and reporting of uncertainty due to discretization in CFD applications," *Journal of Fluids Engineering, Transactions of the ASME,* **130**(7), pp. 780011–780014.

[27] Sousa, J., Paniagua, G., and Saavedra, J., 2017, "Aerodynamic response of internal passages to pulsating inlet supersonic conditions," *Computers and Fluids,* **149**, pp. 31–40.

[28] Goldman, L. J., and Vanco, M. R., 1971, "Computer Program for Design of Two-Dimensional Sharp-Edged-throat Supersonic Nozzle with Boundary-Layer Correction," *NASA*.

[29] Nordeen, C., 2013, "Thermodynamics of a Rotating Detonation Engine," PhD thesis.

[30] Shank, J., King, P., Karnesky, J., Schauer, F., and Hoke, J., 2012, "Development and Testing of a Modular Rotating Detonation Engine," In *50th AIAA Aerospace Sciences Meeting including the New Horizons Forum and Aerospace Exposition*, Aerospace Sciences Meetings. American Institute of Aeronautics and Astronautics, jan.

[31] DeBarmore, N., King, P., Schauer, F., and Hoke, J., 2013, "Nozzle Guide Vane Integration into Rotating Detonation Engine," In *51st AIAA Aerospace Sciences Meeting including the New Horizons Forum and Aerospace Exposition*, Aerospace Sciences Meetings. American Institute of Aeronautics and Astronautics, jan.

[32] Pullan, G., and Adamczyk, J. J., 2017, "Filtering Mixing Planes for Low Reduced Frequency Analysis of Turbomachines," *Journal of Turbomachinery,* **139**(9), apr.

[33] Bruce, P. J. K., and Babinsky, H., 2008, "Unsteady shock wave dynamics," *Journal of Fluid Mechanics,* **603**, pp. 463–473.

[34] Chen, L., Li, J., and Ding, R., 2011, "Identification for the second-order systems based on the step response," *Mathematical and Computer Modelling,* **53**(5), pp. 1074–1083.

[35] Pagendarm H.-G., S. B., 1992, "An Algorithm for Detection and Visualization of Discontinuities in Scientific Data Fields Applied to Flow Data with Shock Waves," In III. Eurographics Workshop in Visualization in Scientific Computing, Viareggio, Italy, 27.-29. April 1992.

[36] Moeckel, W. E., 1949, "Approximate Method for Predicting Form and Location of Detached Shock Waves Ahead of Plane or Axially Symmetric Bodies," In NACA Technical Note.

[37] Tolstov, G. P., 2012, *Fourier series* Courier Corporation.

[38] Nise, N. S., 2020, *Control systems engineering* John Wiley & Sons.

[39] Ghanem, R., Higdon, D., Owhadi, H., and Others, 2017, *Handbook of uncertainty quantification*, Vol. 6 Springer.

[40] Crestaux, T., Le Maıˆtre, O., and Martinez, J.-M., 2009, "Polynomial chaos expansion for sensitivity analysis," *Reliability Engineering System Safety,* **94**(7), pp. 1161–1172.

[41] Hadigol, M., and Doostan, A., 2018, "Least squares polynomial chaos expansion: A review of sampling strategies," *Computer Methods in Applied Mechanics and Engineering,* **332**, pp. 382–407.

[42] Pati, Y. C., Rezaiifar, R., and Krishnaprasad, P. S., 1993, "Orthogonal matching pursuit: recursive function approximation with applications to wavelet decomposition," In Proceedings of 27th Asilomar Conference on Signals, Systems and Computers, pp. 40–44 vol.1.

[43] Stefano, M., and Bruno, S., 2023, UQLab: A Framework for Uncertainty Quantification in Matlab, jan.

[44] Blatman, G., and Sudret, B., 2010, "An adaptive algorithm to build up sparse polynomial chaos expansions for stochastic finite element analysis," *Probabilistic Engineering Mechanics,* **25**(2), pp. 183–197.

[45] van Buuren, R., Kuerten, J. G. M., Geurts, B. J., and Zandbergen, P. J., 1998, "Time accurate simulations of supersonic unsteady flow BT - Sixteenth International Conference on Numerical Methods in Fluid Dynamics," C.-H. Bruneau, ed., Springer Berlin Heidelberg, pp. 326–331.

[46] Shannon, C. E., 1948, "A mathematical theory of communication," *The Bell System Technical Journal,* **27**(3), pp. 379–423.

APPENDIX A: TIME-STEP SELECTION AND PERIODIC CONVERGENCE ANALYSIS

Since Ansys CFX solver is implemented with implicit time integration, the choice of the time step is bounded only by the accuracy required by the solution [45]. Furthermore, Pullan et al. [32] recommend at least 25 time-steps per period to accurately resolve a sinusoidal profile; hence, 40 time-steps were employed to discretize each period and the first 20 harmonics of the inlet fluctuation are captured correctly according to the Whittaker-Shannon sampling theorem [46]. To assess if this sampling frequency is sufficient, the power spectral density (PSD) was calculated

for several variables (Fig. 15a); as the first 5 harmonics contain at least 98% of the total PSD, 40 time-steps per period are considered acceptable for the unsteady simulations.

Periodic convergence of each unsteady simulation was evaluated with Clark's methodology [25]; the selected fuzzy sets compare consecutive periods in terms of time-mean values, amplitude and phase of the fundamental harmonic of the Discrete Fourier Transform (DFT), cross-correlation coefficients at zero lag and fraction of overall signal power at frequencies of interest. Periodic convergence is achieved when the overall fuzzy convergence level, calculated as the minimum between all the fuzzy sets, is above 0.95 for two consecutive cycles. Figure 15b displays the history of periodic convergence for the case with the reference inlet fluctuations; periodic convergence was achieved in six periods for the outlet quantities and for the tangential force on the blade. Nonetheless, each simulation was run at least for 10 periods. Figure 16 shows the complete shock position history for the simulations discussed in Sec. 4.2. It is worth noting that, for the highest frequency case (12000 Hz), two extra time periods were necessary to achieve complete periodic convergence.

APPENDIX B: CALCULATION OF THE CONSTANTS OF A SECOND-ORDER MODEL WITH DIFFERENT POLES

Chen et al. [34] transform the transcendental equation associated to the step-response of a second order model into a system of algebraic equations by evaluating Eq. 11 in the following three specific points: (t1, z(t1)), (2t1, z(2t1)), and (3t1, z(3t1)).

$$z(t) = 1 + \frac{T_3 - T_1}{T_1 - T_2} e^{-t/T_1} - \frac{T_3 - T_2}{T_1 - T_2} e^{-t/T_2} \tag{11}$$

After defining some auxiliary variables (Eq. 12), the system of equations can be easily solved (Eq. 13).

$$\begin{cases} m_1 = e^{-t_1/T_1} \\ m_2 = e^{-t_1/T_2} \\ n = \dfrac{T_3 - T_1}{T_1 - T_2} \\ k_i = z(t_i) - 1 \end{cases} \tag{12}$$

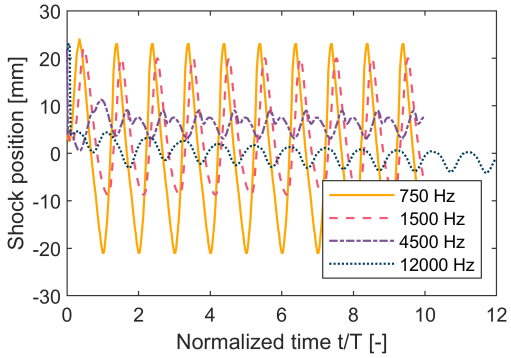

Fig. 16: COMPLETE SHOCK POSITION HISTORY FOR THE CASES PRESENTED IN SEC. 4.2.

$$\begin{cases} m_1 = \dfrac{k_1 k_2 + k_3 + \sqrt{b}}{2(k_1^2 + k_2)} \\ m_2 = \dfrac{k_1 k_2 + k_3 - \sqrt{b}}{2(k_1^2 + k_2)} \\ n = \dfrac{2k_1^3 + 3k_1 k_2 + k_3 - \sqrt{b}}{2\sqrt{b}} \\ b = 4k_1^3 k_3 - 3k_1^2 k_2^2 - 4k_2^3 + k_3^2 + 6k_1 k_2 k_3 \end{cases} \tag{13}$$

Finally, Eq. 14 provides the estimates for the constants T1, T2 and T3.

$$\begin{cases} T_1 = -\dfrac{t_1}{ln(m_1)} \\ T_2 = -\dfrac{t_1}{ln(m_2)} \\ T_3 = n(T_1 - T_2) + T_1 \end{cases} \tag{14}$$

Since the choice of t_1 is arbitrary, this quantity was selected through an iterative procedure which minimizes the error between the model prediction and the CFD step response.

LIST OF FIGURES

LIST OF TABLES